Dual-Band, Orthogonally-Polarized LP-to-CP Converter for SatCom Applications

M. del Mastro, M. Ettorre, A. Grbic

This article has been accepted for publication in a future issue of this journal, but has not been fully edited. Content may change prior to final publication. Citation information: DOI 10.1109/TAP.2020.2989868, IEEE Transactions on Antennas and Propagation

Dual-Band, Orthogonally-Polarized LP-to-CP Converter for SatCom Applications

Michele Del Mastro, Mauro Ettorre, *Senior Member, IEEE*, and Anthony Grbic, *Fellow, IEEE*

***Abstract*—A systematic design of dual-band, orthogonally-polarized linear-to-circular polarization (LP-to-CP) converters is proposed. This class of polarization converters can transform linearly-polarized waves into right- and left-hand circularly-polarized (RHCP and LHCP) waves in two separate non-adjacent frequency bands. The reported polarizer is made of three cascaded bianisotropic sheet admittances, spaced by two isotropic dielectric slabs. The electromagnetic problem is studied by means of impedance boundary conditions. A transmission-matrix analysis of periodically-loaded transmission-lines is employed in design. An analytic model is developed and closed-form expressions are derived for the frequency response of each sheet admittance. This method avoids the use of multi-parameter optimization procedures. An example of a dual-band, orthogonally-polarized LP-to-CP converter is proposed for satellite communication applications in the K/Ka-band. The polarizer separately performs LP-to-LHCP and LP-to-RHCP conversions over the transmitting and receiving channels of the K/Ka-band. The design is validated with a prototype. Under normal incidence, the polarizer exhibits axial ratios (ARs) lower than 3 dB over the 18-22.2 GHz (∼21%) and 28.7-30.4 GHz (∼6%) bands. The total transmission is above -1 dB within the same two bands. The performance is stable for scanning angles up to $\pm 45^{\circ}$. For a 45° angle of incidence, the AR is lower than 3 dB in the bands 17-22 GHz (∼25.6%) and 28.6-30 GHz (∼4.7%) with a total transmission higher than -1.2 dB.**

***Index Terms*—Circular polarization, dual-band polarizer, periodic structures, LP-to-CP conversion, SatCom, metasurfaces.**

I. Introduction

THE demand for high-speed satellite communications (SatCom) calls for ever-increasing robust ground terminal antennas. Circular polarization (CP) is used in satellite links and is a key asset to mitigating multipath fading and polarization mismatch between transmit and receive antennas [1]–[3]. In addition, K/Ka-band SatCom terminals operate in two separate bands: 17.7-21.2 GHz (down-link) and 27.5-31 GHz (up-link). Orthogonal polarizations are preferred in these two bands to improve the isolation between transmitted and received signal.

The design of antennas with orthogonal CPs for the two bands is thus of increasing interest and represents a future challenge for the scientific community.

Manuscript received XX/XX/2018; revised XX/XX/2018. "This work was supported by the Direction Générale de l'Armement and by Brittany Region, France.

M. Del Mastro and M. Ettorre are with Univ. Rennes, CNRS, IETR (Institut d'Électronique et de Télécommunication de Rennes) - UMR 6164, F-35000 Rennes, France (e-mail: michele.delmastro@univ-rennes1.fr).

A. Grbic is with Radiation Laboratory, Department of Electrical Engineering and Computer Science, University of Michigan, Ann Arbor, MI 48109-2122 USA (e-mail: agrbic@umich.edu).

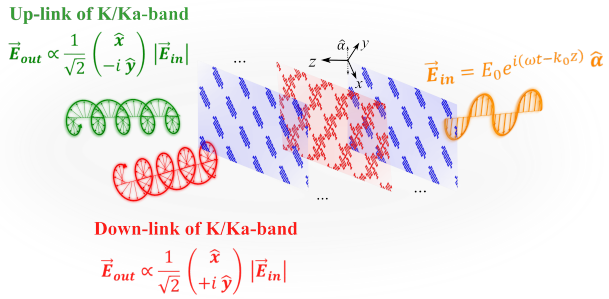

Fig. 1. Exploded view of the dual-band, orthogonally-polarized LP-to-CP converter. The incident waves are linearly polarized at 45° with respect to the orientation of the metal patterns. They are converted into right- and left-hand circularly-polarized waves in two separate bands. The polarizer is a symmetric structure consisting of three patterned metallic claddings (metasurfaces).

The design of highly-efficient dual-band, orthogonally-polarized SatCom antennas is not straightforward. Combining linear-to-circular polarization (LP-to-CP) converters with linearly-polarized (LP) antennas represents a simpler solution that meets the above-mentioned SatCom specifications. Typically, the up- and down-link are covered by combining two distinct radiating apertures with LP-to-CP converters [4]. In this paper, we propose a novel dual-band circular polarizer to attain orthogonal CPs in the K/Ka-band. This solution may be used by a single aperture SatCom terminal covering both bands.

Polarization converters usually consist of cascaded frequency selective surfaces (FSSs) [18]. Multi-layer meander lines or more complex geometries have been designed to achieve broadband, single-band LP-to-CP converters [5]–[8]. Multi-parameter optimizations are usually employed in their design. A semi-analytic method to design single-band LP-to-CP converters has recently been proposed in [9]. As in the design of negative-refractive index (NRI) meta-materials [10], [11], the design procedure in [9] is based on engineering the dispersion of the considered unit cell's phase-shifter. In [9], the unit cell consists of three cascaded metasurfaces. By modeling each metasurface with a given circuit topology, the axial ratio (AR) bandwidth can be broadened, thus reducing insertion losses. However, the works to date [5]–[9] do not provide a systematic procedure to address the design of dual-band LP-to-CP converters with orthogonally-polarized transmission.

The design of dual-band, orthogonally-polarized LP-to-CP converters remains an open area of research. Only a few works can be found in literature. The elements of equivalent circuit models (ECMs) are usually obtained using multi-parameter

This article has been accepted for publication in a future issue of this journal, but has not been fully edited. Content may change prior to final publication. Citation information: DOI 10.1109/TAP.2020.2989868, IEEE Transactions on Antennas and Propagation

optimizations. The goal is to maximize the transmission at two frequencies and shape the AR response according to the project specifications. Multi-layer FSS-based structures have been proposed operating either in reflection [19]–[23] or transmission [24], [25]. In [25], the entries of ECMs are obtained by performing optimizations in Keysight Advanced Design System (ADS) [28]. The ECMs of [24] have been recently presented in [26], but they refer to a given unit cell's geometry. Generic ECMs irrespective of unit cell's geometry have not been presented yet. Alternatively, all-dielectric cascaded metasurfaces can achieve multi-band, multi-functional polarization controllers [29], [30]. Such low-loss topologies are very attractive but in general thicker than cascades of patterned metallic surfaces. The solution proposed in [31] combines a four layer meander line polarizer with a polarization rotator, but the final system is bulky. Finally, exploiting the real-time re-configurable properties offered by time-modulated metasurfaces would be a further way to realize dual-band, orthogonally-polarized LP-to-CP converters, as was done for polarization rotators in [33]. However, no prototype has been presented in the open literature yet.

The goal of this contribution is to provide a fully analytic design procedure for dual-band, orthogonally-polarized LP-to-CP metasurface-based converters. A dual-band quarter-wave plate is realized by cascading three anisotropic electric sheet admittances, separated by two isotropic dielectric slabs. As shown in Fig. 1, 45°-slanted LP plane-waves are converted to left- and right-hand circularly-polarized waves in the down- and up-link channels of K/Ka-band SatCom link. The problem is studied by considering two equivalent shunt-loaded transmission line (TL) problems for each transverse field component (i.e., x- and y-polarized waves). The desired polarization conversion is achieved by enforcing 100% transmission at two design frequencies in the two considered bands. A $\pm 90^\circ$ phase delay is also enforced between the two transmitted transverse components to achieve orthogonal CPs to the two bands. The proposed ECMs are fully characterized using analytic formulae.

The paper is organized as follows. The design procedure is outlined in Section II. Section III proposes the design of a dual-band, orthogonally-polarized LP-to-CP converter in the K/Ka-band. The design is validated by a prototype in Section IV and its performance is compared with the state-of-the-art. Section V discusses the capability and the limitations of the presented analytic model. Finally, Section VI concludes the paper.

II. Analytic Model

A LP-to-CP converter is also referred to as a quarter-wave plate [12]. The transverse field components are phased $\pm 90^\circ$ with respect to each other while maintaining equal amplitudes. Fig. 2 shows the geometry of the considered unit cell's phase-shifter. It consists of three sheet admittances cascaded along z-axis. Two dielectric slabs of thickness d and relative dielectric constant ϵ_r are used to separate the sheets. The transverse extent of the structure is assumed infinite. The outer sheets $\bar{\bar{Y}}_{s1}$ are diagonal and equal to each other. The inner admittance $\bar{\bar{Y}}_{s2}$

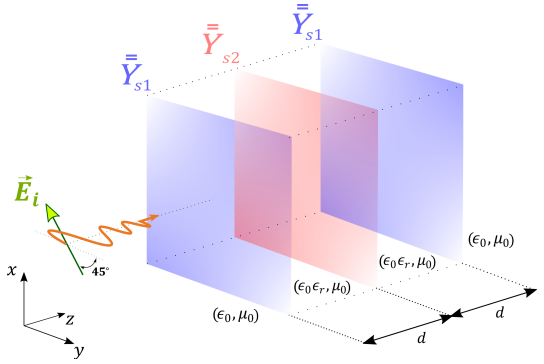

Fig. 2. Geometry of the problem under analysis. Three anisotropic sheet admittances are cascaded along the z-axis. The external sheet admittances are equal.

is also diagonal but distinct. The electric admittance of each sheet is given by

$$\bar{\bar{Y}}_{sn} = \begin{bmatrix} Y_{sn}^{xx} & 0 \\ 0 & Y_{sn}^{yy} \end{bmatrix}, \quad n = \{1, 2\} \tag{1}$$

Given that the admittances are diagonal, the structure in Fig. 2 can be analyzed by considering each orthogonal transverse component separately. To streamline the mathematical formulation, we will consider scalar admittances hereinafter.

A. ABCD matrix formulation

The structure in Fig. 2 can be seen as the unit cell of periodic structure consisting of a transmission line (TL) loaded with reactive elements. Therefore, the theory of two-port microwave networks can be used in the analysis [15]. Let us assume that the admittance matrix of such a network is symmetric (reciprocal) and its entries are purely imaginary quantities (lossless). Each sheet admittance can be expressed in terms of the Bloch phase delay ϕ of the unit cell. To this end, the transmission matrix of the unit can be computed [15]

$$\begin{bmatrix} A & B \\ C & D \end{bmatrix} = \begin{bmatrix} A_1 & B_1 \\ C_1 & D_1 \end{bmatrix} \begin{bmatrix} 1 & 0 \\ Y_{s2} & 1 \end{bmatrix} \frac{1}{\xi} \begin{bmatrix} D_1 & B_1 \\ C_1 & A_1 \end{bmatrix} \tag{2}$$

where

$$\begin{bmatrix} A_1 & B_1 \\ C_1 & D_1 \end{bmatrix} = \begin{bmatrix} 1 & 0 \\ Y_{s1} & 1 \end{bmatrix} \begin{bmatrix} \cos\theta & i\eta_d \sin\theta \\ \frac{i \sin\theta}{\eta_d} & \cos\theta \end{bmatrix} \tag{3}$$

where θ is the electrical length of each dielectric slab and $\eta_d = \eta_0/\sqrt{\epsilon_r}$, where η_0 is the characteristic impedance of free-space. Moreover, $\xi = det\left\{\begin{bmatrix} A_1 & B_1 \\ C_1 & D_1 \end{bmatrix}\right\} = A_1 D_1 - B_1 C_1$, where $det\{\cdot\}$ indicates the determinant of a matrix.

Finally, the inner and outer sheet admittances can both be expressed in closed formulae as function of Bloch impedance Z_B and Bloch phase delay ϕ of the unit cell in Fig. 2. After some algebraic manipulations and exploiting the symmetry of the network [16], we obtain

$$Y_{s1} = \frac{i}{\eta_d}\left(\cot\theta - \frac{\eta_d}{Z_B}\cot(\phi/2)\right) \tag{4}$$

$$Y_{s2} = \frac{i}{\eta_d}\left(2\cot\theta - \frac{Z_B}{\eta_d}\csc^2\theta \sin\phi\right) \tag{5}$$

This article has been accepted for publication in a future issue of this journal, but has not been fully edited. Content may change prior to final publication. Citation information: DOI 10.1109/TAP.2020.2989868, IEEE Transactions on Antennas and Propagation

A detailed derivation of equations (4) and (5) is reported in Appendix A.

B. Maximum transmission condition

The transmission coefficient S_{21} of the unit cell in Fig. 2 is given by

$$S_{21} = \left(\cos\phi + i\frac{\sin\phi}{2}\left(\frac{Z_B}{\eta_0} + \frac{\eta_0}{Z_B}\right) \right)^{-1} \tag{6}$$

Transmission is maximized by setting $|S_{21}| = 1$ in (6), yielding

$$\frac{Z_B}{\eta_0} + \frac{\eta_0}{Z_B} = 2 \quad \Rightarrow \quad Z_B = \eta_0 \tag{7}$$

Equation (7) shows that the network exhibits maximum transmission when impedance is matched to free-space. This result is easy to understand being equivalent to the zero reflection condition in TL theory [15], [17]. It is important to note that equation (7) does not necessarily lead to maximum efficiency [17].

Finally, substituting (7) into (4) and (5) provides the sheet admittance values for 100% transmission regime

$$B_{s1}(\phi, f) = \Im\{Y_{s1}\} = \frac{1}{\eta_d}\left(\cot\theta - \frac{\cot(\phi/2)}{\sqrt{\epsilon_r}}\right) \tag{8}$$

$$B_{s2}(\phi, f) = \Im\{Y_{s2}\} = \frac{1}{\eta_d}\left(2\cot\theta - \sqrt{\epsilon_r}\csc^2\theta\sin\phi\right) \tag{9}$$

C. Design procedure

The design procedure for dual-band, orthogonally-polarized LP-to-CP converters starts by specifying an appropriate frequency behavior for each electric sheet admittance. Once this is done, the design work-flow consists of enforcing the maximum transmission condition (7) at two distinct design frequencies: f_{01} and f_{02}. The systematic method depends on the variable ϕ_{01}^{xx}, i.e. the Bloch phase delay of the unit cell in Fig. 2 for x-polarized waves at frequency f_{01}. ϕ_{01}^{xx} is the only required input parameter to the model. After assuming a value for ϕ_{01}^{xx}, equations (8) and (9) are used to compute the sheet susceptances $B_{s1,01}^{xx} = B_{s1}^{xx}(\phi_{01}^{xx}, f_{01})$ and $B_{s2,01}^{xx} = B_{s2}^{xx}(\phi_{01}^{xx}, f_{01})$ at frequency f_{01}. The frequency response of Y_{s1}^{xx} is assumed to be that of an inductor or capacitor. According to the sign of $B_{s1,01}^{xx}$, the outer sheet admittance for x-polarized waves Y_{s1}^{xx} is expressed as a function of the frequency, as follows

$$Y_{s1}^{xx} = \begin{cases} i\omega C_{s1}^{xx}, & if \quad B_{s1,01}^{xx} > 0 \\ (i\omega L_{s1}^{xx})^{-1}, & if \quad B_{s1,01}^{xx} < 0 \end{cases} \tag{10}$$

where

$$C_{s1}^{xx} = B_{s1,01}^{xx}/\omega_{01} \tag{11}$$

$$L_{s1}^{xx} = \left(\omega_{01}|B_{s1,01}^{xx}| \right)^{-1} \tag{12}$$

where ω is the angular frequency and $\omega_{01} = \omega(f_{01})$.

Next, the phase delay for x-polarized fields ϕ_{02}^{xx} is obtained by inverting (8) at the frequency f_{02}, resulting in

$$\phi_{02}^{xx} = 2\arctan\left(\frac{1}{\sqrt{\epsilon_r}\cot\theta_{02} - \eta_0 B_{s1,02}^{xx}}\right) \tag{13}$$

where $\theta_{02} = \theta(f_{02})$ and $B_{s1,02}^{xx} = B_{s1}^{xx}(\phi_{02}^{xx}, f_{02})$ is calculated by inverting (10) at the frequency f_{02}. It is worth noticing that this procedure may be repeated assuming the frequency response of Y_{s2}^{xx} is that of a single lumped reactive element. This calculation is straightforward and not reported here for the sake of brevity.

Once ϕ_{01}^{xx} and ϕ_{02}^{xx} are known, we enforce the phase delay for y-polarized waves to be $\pm 90°$ and $\mp 90°$ shifted with respect to x-polarized fields at the two design frequencies f_{01} and f_{02}, respectively. It follows

$$\phi_{01}^{yy} = \phi_{01}^{xx} \pm 90° \tag{14}$$

$$\phi_{02}^{yy} = \phi_{02}^{xx} \mp 90° \tag{15}$$

Enforcing (14) and (15) guarantees orthogonal LP-to-CP conversions at the two design frequencies. At this point, equation (13) is inserted into (9) and $B_{s2}^{xx}(\phi_{02}^{xx}, f_{02})$ is calculated at the frequency f_{02}. Likewise, B_{s1}^{yy} and B_{s2}^{yy} are computed at the two design frequencies, by substituting both (14) and (15) into (8) and (9), respectively. Thus, the frequency responses of Y_{s2}^{xx}, Y_{s1}^{yy}, and Y_{s2}^{yy} are assumed to be those of series-LC resonators, yielding

$$Y_{s1}^{yy} = \left(i\omega L_{s1}^{yy} + \frac{1}{i\omega C_{s1}^{yy}}\right)^{-1} \tag{16}$$

$$Y_{s2}^{xx} = \left(i\omega L_{s2}^{xx} + \frac{1}{i\omega C_{s2}^{xx}}\right)^{-1} \tag{17}$$

$$Y_{s2}^{yy} = \left(i\omega L_{s2}^{yy} + \frac{1}{i\omega C_{s2}^{yy}}\right)^{-1} \tag{18}$$

where

$$C_{sm}^{\psi\psi} = \begin{cases} \frac{|B_{sm,01}^{\psi\psi}|\left(1-\Delta f^2\right)}{\omega_{01}\left(1+\Delta f|\Delta B_{sm}^{\psi\psi}|\right)}, & if \quad \begin{matrix} B_{sm,01}^{\psi\psi} > 0 \\ B_{sm,02}^{\psi\psi} < 0 \end{matrix} \\ \frac{|B_{sm,01}^{\psi\psi}|\left(1-\Delta f^2\right)}{\omega_{01}\left(1-\Delta f|\Delta B_{sm}^{\psi\psi}|\right)}, & if \quad 0 < B_{sm,01}^{\psi\psi} < B_{sm,02}^{\psi\psi} \\ -\frac{|B_{sm,01}^{\psi\psi}|\left(1-\Delta f^2\right)}{\omega_{01}\left(1-\Delta f|\Delta B_{sm}^{\psi\psi}|\right)}, & if \quad B_{sm,01}^{\psi\psi} < B_{sm,02}^{\psi\psi} < 0 \end{cases} \tag{19}$$

$$L_{sm}^{\psi\psi} = \begin{cases} \frac{|B_{sm,01}^{\psi\psi}| - \omega_{01}C_{sm}^{\psi\psi}}{\omega_{01}^2 C_{sm}^{\psi\psi}|B_{sm,01}^{\psi\psi}|}, & if \quad \begin{matrix} B_{sm,01}^{\psi\psi} > 0 \\ B_{sm,02}^{\psi\psi} < 0 \\ C_{sm}^{\psi\psi} < |B_{sm,01}^{\psi\psi}|/\omega_{01} \end{matrix} \\ \frac{|B_{sm,01}^{\psi\psi}| - \omega_{01}C_{sm}^{\psi\psi}}{\omega_{01}^2 C_{sm}^{\psi\psi}|B_{sm,01}^{\psi\psi}|}, & if \quad \begin{matrix} 0 < B_{sm,01}^{\psi\psi} < B_{sm,02}^{\psi\psi} \\ C_{sm}^{\psi\psi} < |B_{sm,01}^{\psi\psi}|/\omega_{01} \end{matrix} \\ \frac{|B_{sm,01}^{\psi\psi}| + \omega_{01}C_{sm}^{\psi\psi}}{\omega_{01}^2 C_{sm}^{\psi\psi}|B_{sm,01}^{\psi\psi}|}, & if \quad B_{sm,01}^{\psi\psi} < B_{sm,02}^{\psi\psi} < 0 \end{cases} \tag{20}$$

where

$$m = \begin{cases} 2, & if \quad \psi = x \\ \{1, 2\}, & if \quad \psi = y \end{cases} \tag{21}$$

and $\Delta f = f_{01}/f_{02}$, $\Delta B_{sm}^{\psi\psi} = B_{sm,01}^{\psi\psi}/B_{sm,02}^{\psi\psi}$ where $B_{sm,01}^{\psi\psi} = B_{sm}^{\psi\psi}(\phi_{01}^{\psi\psi}, f_{01})$ and $B_{sm,02}^{\psi\psi} = B_{sm}^{\psi\psi}(\phi_{02}^{\psi\psi}, f_{02})$.

This article has been accepted for publication in a future issue of this journal, but has not been fully edited. Content may change prior to final publication. Citation information: DOI 10.1109/TAP.2020.2989868, IEEE Transactions on Antennas and Propagation

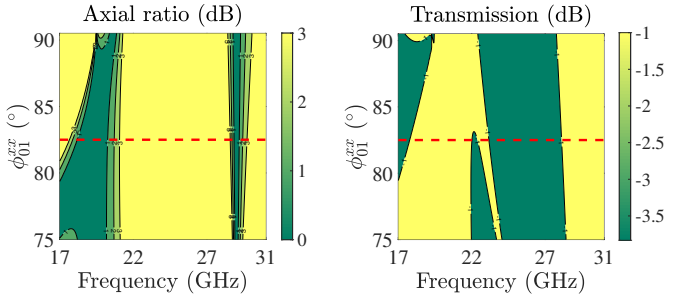

(a) (b)

Fig. 3. Contour plots of the absolute value of (a) axial ratio and (b) transmission coefficient as a function of frequency and ϕ_{01}^{xx}. The dashed red line indicates the chosen operating point for the design.

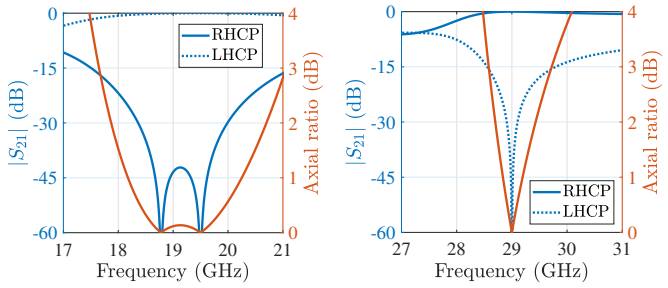

(a) Down-link of K/Ka-band. (b) Up-link of K/Ka-band.

Fig. 4. Numerical results for the dual-band, orthogonally-polarized LP-to-CP converter with $\phi_{01}^{xx} = 82.5°$. Axial ratio and transmission coefficients for both RHCP and LHCP are plotted in two bands: (a) 17-21 GHz and (b) 27-31 GHz.

To summarize, this model only requires the phase delay for x-polarized waves ϕ_{01}^{xx} as an input parameter. The bandwidths are maximized by sweeping ϕ_{01}^{xx} and observing its impact on the AR and the transmission. This is a direct consequence of having modeled Y_{s1}^{xx} as a single shunt inductor or capacitor. It is worth noting that a LC-series topology could be chosen for Y_{s1}^{xx} as well. The latter would provide two design parameters, namely ϕ_{01}^{xx} and ϕ_{02}^{xx}. This scenario would require a more complex approach (e.g., optimizations) to search for the best values for ϕ_{01}^{xx} and ϕ_{02}^{xx}. Besides, inductors and capacitors are easier to design than resonators using patterned metallic claddings.

III. Dual-band, Orthogonally-Polarized LP-to-CP Converter for SatCom Applications

Here, a design example is reported and discussed. The goal is to design a dual-band LP-to-CP converter for next generation SatCom terminal antennas. Such device is required to attain polarization diversity between the down-link (17.7-21.2 GHz) and the up-link (27.5-31 GHz) communication channels in the K/Ka-band. We enforce a LP-to-LHCP conversion in the lower frequency band, as well as a LP-to-RHCP conversion in the upper band. In the following, the bandwidth of the polarizer will be referred to as the frequency range over which the AR $<$ 3 dB and the transmission is higher than -1 dB.

Using the model proposed in Section II, we will first focus on retrieving all the design parameters. Afterwards, a physical realization of the sheets is proposed and discussed. Each sheet is realized as a sub-wavelength textured metallic cladding: a metasurface [13], [14].

A. Numerical results based on ECMs

As detailed in Section II, we will focus on a class of polarizers consisting of three metasurfaces, separated by two isotropic dielectric slabs [14]. Two Rogers RO3003™ panels ($\epsilon_r = 3.00$, $\tan\delta = 0.0010$ @ 10 GHz) of thickness $d = 1.524$ mm are used as dielectric substrates. They are bonded together using Taconic FastRise™ FR-27-0030-25 (F) ($\epsilon_r = 2.72$, $\tan\delta = 0.0014$ @ 10 GHz) of $\sim 80\mu m$ pressed thickness. The overall thickness of the polarizer is approximately 3.145 mm. The design frequencies are $f_{01} = 19.5$ GHz and $f_{02} = 29$ GHz.

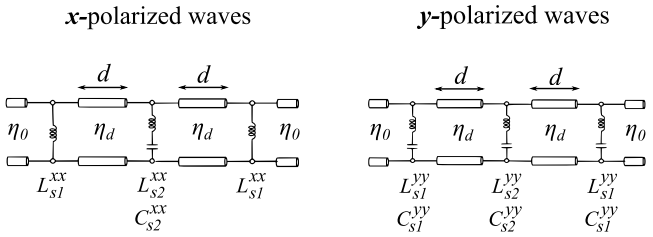

Fig. 5. Equivalent circuit models of the structure. Networks for x- and y-polarized waves are analyzed separately.

As mentioned earlier, the only parameter the designer sets is ϕ_{01}^{xx}. In fact, a single reactive element is employed to describe the frequency response of the admittance sheet Y_{s1}^{xx}. Thus, the parameter ϕ_{02}^{xx} is not a degree of freedom in the model, but is computed from (13). Given an incident LP plane-wave with E-field polarized in the direction $(\hat{x} \pm \hat{y})/\sqrt{2}$, the impact of the choice of ϕ_{01}^{xx} on AR and transmission bandwidths is observed. By enforcing LHCP in (14) and RHCP in (15), contour plots of the AR and the transmission are shown in Fig. 3. Values of ϕ_{01}^{xx} within the range $[75°, 90.5°]$ lead to dual-band LP-to-CP conversions with orthogonal CP functionality. Unlike in [13], a 360°-phase coverage is not achieved while designing multi-band polarization converters. Furthermore, different bandwidths result from distinct values of ϕ_{01}^{xx}. Considering the trade off, a phase delay of $\phi_{01}^{xx} = 82.5°$ is chosen. This operating point is in the middle of the range of solutions $[75°, 90.5°]$, as graphically depicted by a dashed red line in Fig. 3. It offers large bandwidths and robustness of the system to tolerances.

The corresponding AR and transmission coefficients are plotted in Fig. 4. Specifically, the polarizer conveys LHCP and RHCP fields in the frequency bands 17.6-21 GHz and 28.5-29.7 GHz, respectively. The model of Section II has been used to predict the frequency behavior of each sheet admittance. All sheet admittances can thus be studied by means of ECMs, as depicted in Fig. 5 for x- and y-polarized waves. Y_{s1}^{xx} is modeled as a shunt inductor, whereas series-LC resonators model the remaining sheet admittances. For the sake of completeness, the values of the lumped circuit elements are listed in Table I.

This article has been accepted for publication in a future issue of this journal, but has not been fully edited. Content may change prior to final publication. Citation information: DOI 10.1109/TAP.2020.2989868, IEEE Transactions on Antennas and Propagation

TABLE I
CIRCUIT ELEMENTS OBTAINED BY USING THE ANALYTIC METHOD PROPOSED IN SECTION II

	Outer sheets $(n=1)$	**Inner sheet** $(n=2)$	
C_{sn}^{xx}	n.a.	20.5	(fF)
C_{sn}^{yy}	6.97	12.3	
L_{sn}^{xx}	14.5	4.80	(nH)
L_{sn}^{yy}	5.98	3.10	

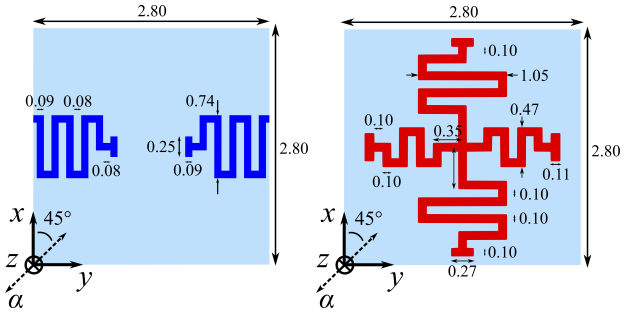

(a) Outer sheets' unit cell. (b) Inner sheet's unit cell.

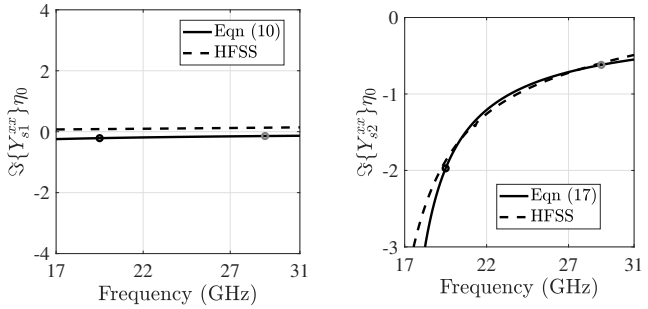

(c) Outer sheets: x-pol fields. (d) Inner sheet: x-pol fields.

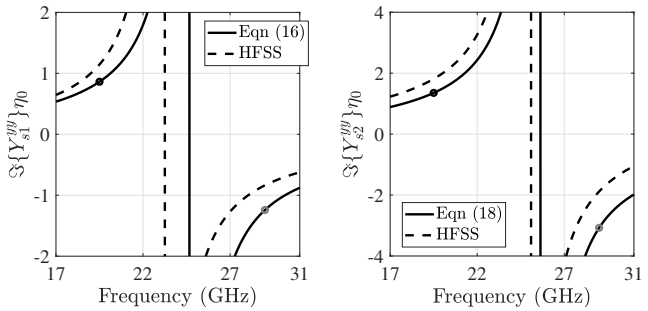

(e) Outer sheets: y-pol fields. (f) Inner sheet: y-pol fields.

Fig. 6. Patterned metallic geometries of the metasurfaces' unit cell: (a) outer and (b) inner sheets. All dimensions are given in millimeters. The simulated susceptances for the patterned metallic geometries are shown in (c)-(e) for x- and (d)-(f) for y-polarized fields. The black and grey dot markers indicate the desired design values at the frequency f_{01} and f_{02}, respectively.

B. Physical design and full-wave results

Each sheet admittance is realized with periodic sub-wavelength patterned metallic cladding [18]. The unit cell's shape and geometrical sizes were designed through full-wave simulations in ANSYS HFSS 2018.2 [36]. The simulation setup can be found in [14]. The first two fundamental Floquet modes excite the unit cell, whose sides are surrounded by periodic boundary conditions. The frequency responses are

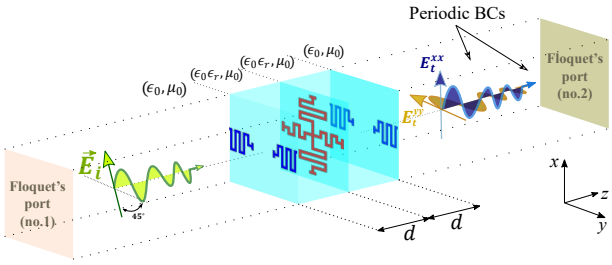

(a) Simulation setup.

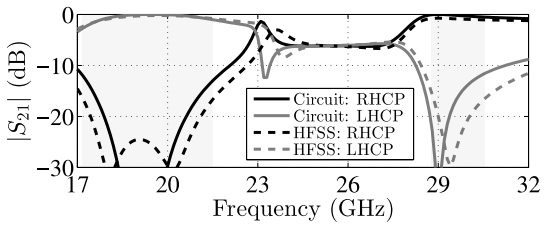

(b) Transmitted coefficients.

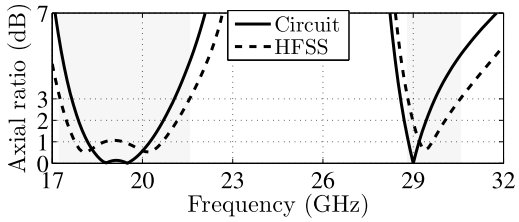

(c) Axial ratio.

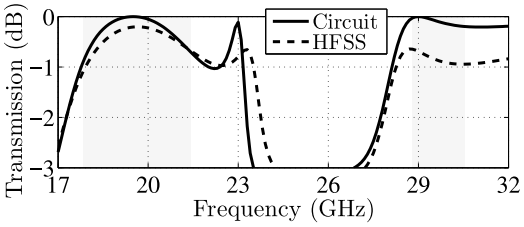

(d) Total transmission.

Fig. 7. (a) Simulation setup of the polarizer's unit cell. A comparison between the circuit network and full-wave simulations [36] is reported. (b) Transmitted LHCP and RHCP. (c) Axial ratio. (d) Total transmission. The full-wave simulations considers a normal incidence onto the polarizer. Besides, the incident E-field is linearly-polarized in the direction $\hat{\alpha} = (\hat{x} \pm \hat{y})/\sqrt{2}$.

then extracted from the reflection coefficient [14] for both x- and y-polarized fields and matched to those of the ECMs in Fig. 5. The choice of the unit cell's geometry is inspired by standard Jerusalem cross shapes, whose simplified ECM consists of series-LC resonators [37], [38]. The proposed geometries are shown in Figs. 6(a) and 6(b). The metasurface's transverse cell dimensions are $0.28\lambda_{min} \times 0.28\lambda_{min}$, where λ_{min} is the free-space wavelength at 31 GHz. Gap capacitors are designed in combination with meandered lines, to attain the circuit elements in Table I. Their susceptances are plotted in Figs. 6(c) to 6(f) for normal incidence in the frequency band 17-31 GHz. The desired susceptance values ((8) and (9)) are also plotted using black and grey dot markers at the frequencies f_{01} and f_{02}, respectively. Very good agreement between ECMs and full-wave simulations is observed. No optimization process was performed in the design. It is worth

This article has been accepted for publication in a future issue of this journal, but has not been fully edited. Content may change prior to final publication. Citation information: DOI 10.1109/TAP.2020.2989868, IEEE Transactions on Antennas and Propagation

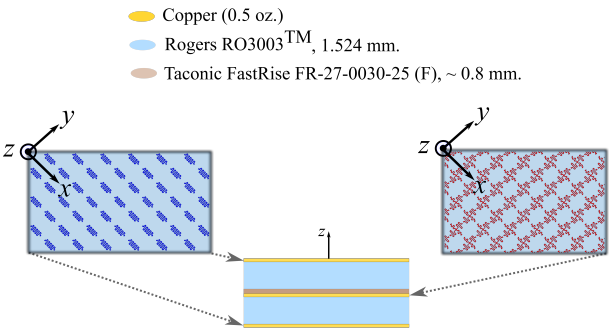

(a) Cross section of the polarizer.

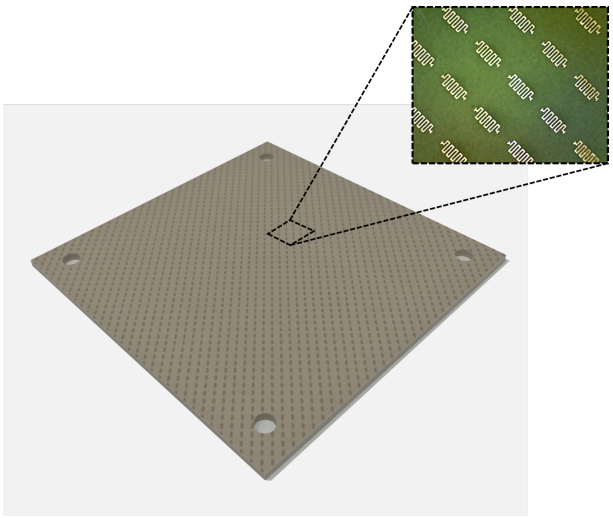

(b) Fabricated prototype.

Fig. 8. (a) PCB stack-up of the polarizer. (b) Fabricated prototype. The overall size of the board is $123.74 \times 123.74 \times 3.14$ mm^3. The outer metal pattern is highlighted by a zoomed-in photograph's detail.

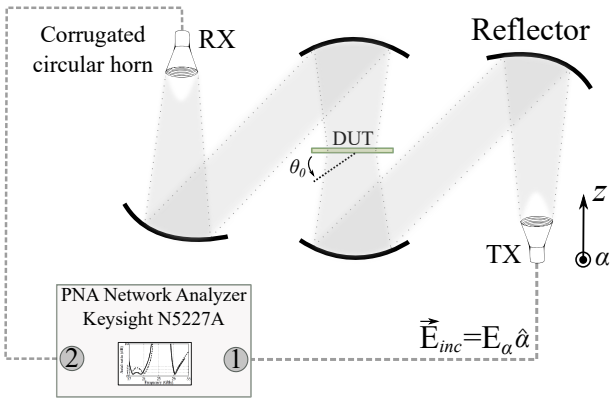

(a)

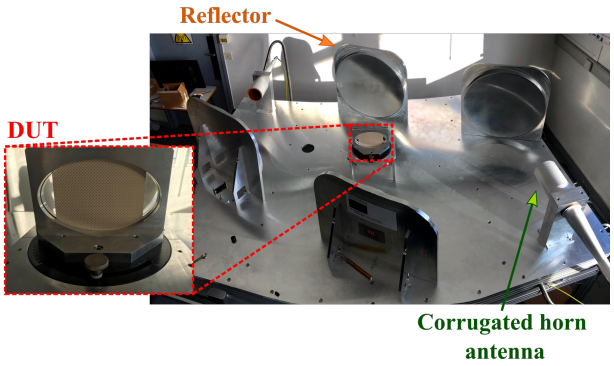

(b)

Fig. 9. (a) Schematic drawing of the experimental setup used to measure the polarizer: quasi-optical test-bench [39]. (b) Photograph of the test setup.

noting that in Fig. 6(c) the large inductance L_{s1}^{xx} is realized as a very small capacitor. In terms of physical design, there is no metal pattern along x-axis for the outer sheets (see Fig. 6(a)). This is only possible when the sheet admittance approaches the open condition, as follows

$$Y_{s1}^{xx} \xrightarrow{C_{s1}^{xx}\to 0 \;\; or \;\; L_{s1}^{xx}\to +\infty} 0 \tag{22}$$

Finally, the full-wave simulation setup is depicted in Fig. 7(a). The stack-up of the polarizer is simulated as a structure that is transversely periodic. The illumination consists of a LP plane-wave with the E-field polarized in the direction $\hat{\alpha} = (\hat{x} \pm \hat{y})/\sqrt{2}$. Normal incidence is considered in the simulations. Fig. 7(b) shows that a LP-to-LHCP conversion is performed in the lower band and LP-to-RHCP in the upper band. The simulated AR is plotted in Fig. 7(c). The 3-dB-AR bandwidths are 22% (17.2-21.6 GHz) and 6% (28.8-30.6 GHz). The transmission coefficient is plotted in Fig. 7(d). The designed polarizer exhibits larger 3-dB-AR bandwidths than its ECM. The transmission is 0.7 dB lower than the ECM results in the upper band (see Fig. 7(d)). This is due to a difference between ECMs and physical design. In fact, the outer metasurface's unit cell and ECM have a different circuit topology for x-polarized waves, see Fig. 6(c). However, the transmission is acceptable since it is above -1 dB everywhere in the bands of interest.

IV. Prototype and Experimental Results

Several prototypes were fabricated, using standard printed circuit board (PCB) technology. A schematic representation of the converter cross section is depicted in Fig. 8(a). The patterned metallic surfaces are etched on the faces of the substrates, with a 45°-rotated orientation with respect to the circuit board edges. A photograph of the fabricated board is shown in Fig. 8(b). The transverse size of the converter is $\sim 7\lambda_{max}$, where λ_{max} is the free-space wavelength at 17 GHz. The overall dimension of the polarizer is $123.74 \times 123.74 \times 3.14$ mm^3. As shown in Fig. 8(b), the inner textured metal cladding is not visible.

A. Measurement setup

The dual-band, orthogonally-polarized LP-to-CP converter was experimentally characterized using a quasi-optical measurement system (Thomas Keating Ltd) [39]. A schematic drawing of the experimental setup is shown in Fig. 9. The fabricated boards are illuminated by a collimated Gaussian beam, under normal and oblique incidence. Specifically, two corrugated circular-horn antennas are employed for illumination and reception. The first horn (TX in Fig. 9) feeds

This article has been accepted for publication in a future issue of this journal, but has not been fully edited. Content may change prior to final publication. Citation information: DOI 10.1109/TAP.2020.2989868, IEEE Transactions on Antennas and Propagation

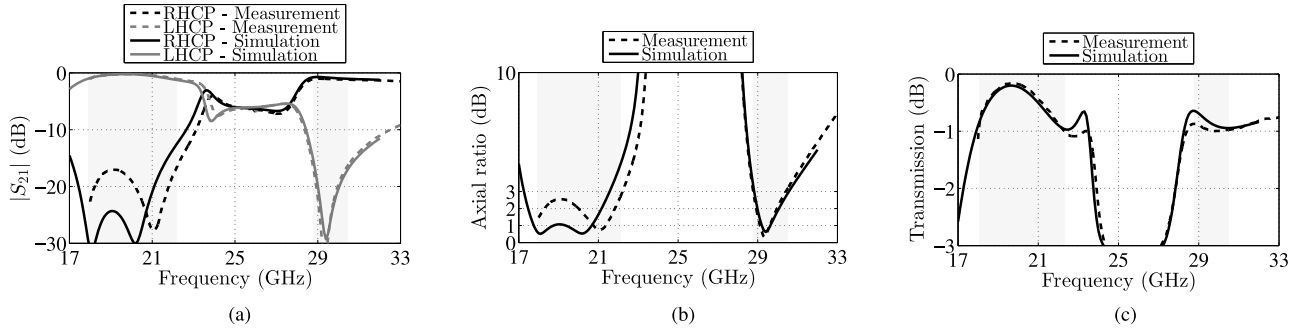

Fig. 10. Comparison between measured and full-wave performance of the polarizer. (a) Transmitted LHCP and RHCP. (b) Axial ratio. (c) Total transmission of the polarization converter. The measurements refer to a normal illumination of the DUT.

a pair of reflectors, whose purpose is to focus the incident Gaussian beam on the device under test (DUT). A second pair of reflectors focuses the field coming from the sample to a receiving corrugated circular-horn antenna (RX in Fig. 9). The horns are connected to a PNA network analyzer (Keysight N5227A) with coaxial cables. The experiments in the band 17-31 GHz were carried out considering two separate measurement setups to cover the two bands 18-26 GHz and 26-40 GHz, respectively.

A free-space thru, reflect, line (TRL) calibration procedure is performed to calibrate the input ports located at the interfaces of the coaxial cables. The effects of waveguide transitions and horn-antennas are not calibrated out, but a time-gating procedure is applied to isolate the DUT. The transmission coefficients are measured by rotating the receiving horn in the direction of the x- and y-axis (see Fig. 8(a)). The DUT is characterized in terms of its scattering matrix. Finally, the AR and the transmitted power are calculated by post-processing the measured data.

B. Measured results for normal incidence

The measured results are plotted in Fig. 10, when the DUT is illuminated under normal incidence. As shown in Fig. 10(a), the dual-band and the orthogonally-polarized transmission of the polarizer have been demonstrated. A $45°$-slanted LP plane-wave is transformed into LHCP and RHCP plane-waves in two separate bands. The CP's purity is characterized in terms of AR, whose plot is shown in Fig. 10(b). Also, the total efficiency of the polarizer is plotted in Fig. 10(c). Several experiments were performed on four fabricated boards. The measured results were in excellent agreement with full-wave simulations, thus demonstrating the reliability of fabrication and measurement processes. A slight frequency shift exists between the measured and simulated results at lower frequencies. This is likely due to a phase variation resulting from fabrication tolerances. From Fig. 10(c) it is evident that the measured transmitted power matches very well in amplitude with simulations. This points to the fact that there is a phase mismatch at lower frequencies between measurement and simulation. Fig. 11(a) compares the phase difference $\Delta\phi = \phi^{yy} - \phi^{xx}$ in measurement and simulation. A percentage variation of more than 10% occurs between the measured and

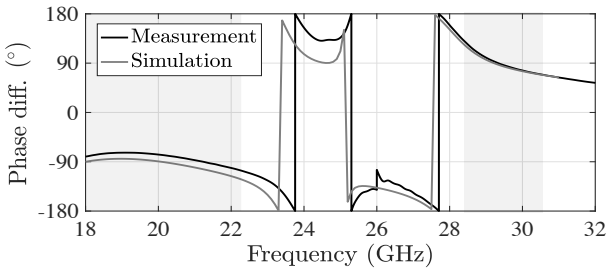

(a) Phase difference $\Delta\phi = \phi^{yy} - \phi^{xx}$.

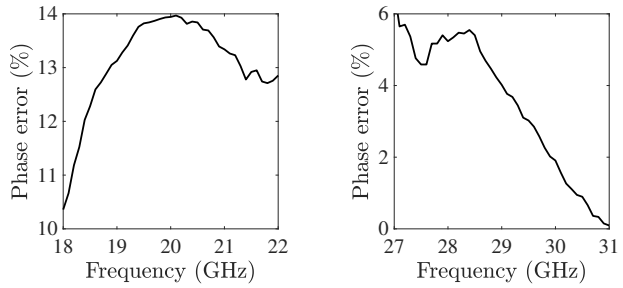

(b) Downlink of K/Ka-band. (c) Uplink of K/Ka-band.

Fig. 11. (a) Phase difference $\Delta\phi = \phi^{yy} - \phi^{xx}$ comparison between measurements and simulations. Percentage error of measured data in the (a) downlink and (b) uplink of the K/Ka-band.

simulated phase difference $\Delta\phi$ at lower frequencies, whereas such a difference is lower than 5% in the upper band, as shown in Figs. 11(b) and (c). This difference is likely due to fabrication tolerances. Indeed, tolerances in the substrate's thickness d impact the electrical paths of the propagating waves. Likewise, variations in the dielectric constant ϵ_r result in different refraction behaviors. In both cases, the phase delay ϕ may vary with respect to the design value. These effects can be observed using ECMs in Section II. Figs. 12(a) and (b) show the AR variation when fabrication tolerances are considered for d and ϵ_r, respectively. The tolerances $\delta_{toll} = 0.0762$ mm and $\delta_{r,toll} = 0.04$ are provided by Rogers Corporation [40]. It is clear from Fig. 12 that tolerances in d and ϵ_r cause a frequency shift at lower frequencies. The AR response remains nearly unvaried in the upper band. Therefore, the AR response exhibits a more robust stability to tolerances at higher frequencies than at lower. This behavior

This article has been accepted for publication in a future issue of this journal, but has not been fully edited. Content may change prior to final publication. Citation information: DOI 10.1109/TAP.2020.2989868, IEEE Transactions on Antennas and Propagation

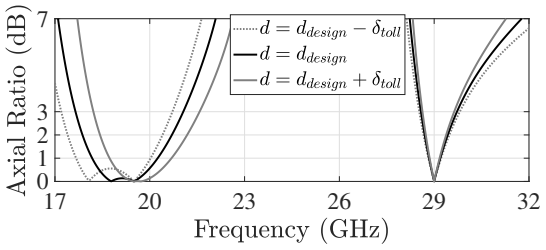

(a) Tolerances of the substrate's thickness.

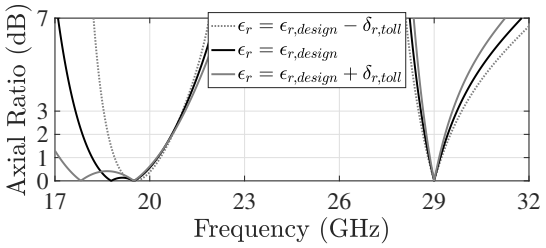

(b) Tolerances of the substrate's dielectric constant.

Fig. 12. Tolerances effects of (a) d and (b) ϵ_r on AR using ECMs. The nominal values of d and ϵ_r are varied by fabrication tolerances provided by Rogers Corporation [40].

TABLE II
MEASURED FRACTIONAL BANDWIDTHS OF THE PROPOSED DUAL-BAND, ORTHOGONALLY-POLARIZED LP-TO-CP CONVERTER UNDER NORMAL PLANE-WAVE INCIDENCE

	LHCP	**RHCP**	
Axial ratio (< 3 dB)	[17, 22.2]	[28.7, 30.4]	(GHz)
Transmission (> -1 dB)	[18, 22.3]	[28.4, 31]	
Total relative bandwidth	~ 21	~ 6	(%)

* Total bandwidth: AR $<$ 3 dB and transmission better than -1 dB.

at lower frequencies is attributed to the presence of two close resonances in the transmission coefficient response (see Fig. 10(a)). Small variations of the phase delay in the structure (see Fig. 2) have a stronger impact on shifting the resonances. On the other hand, only one resonance appears in the upper band, as shown in Fig. 10(a). A more robust frequency behavior is then expected in this case. This effect is confirmed by the measurements shown in Fig. 10(b).

To conclude, the performance of the converter is summarized in Table II. The polarizer performs a LP-to-LHCP conversion over a 21% fractional bandwidth. Furthermore, a LP-to-RHCP conversion is performed over a 6% fractional bandwidth. These bandwidths are calculated considering a transmission higher than -1 dB.

C. Measured results for oblique incidence

The fabricated boards were also tested under oblique incidence. The DUT is mechanically-rotated on the quasi-optical test-bench. The impinging waves illuminate the DUT at different angles θ_0, as shown in Fig. 9. Specifically, two types of illuminations were considered. In the first scenario, the impinging plane-wave presents the E-field polarized along the $\hat{\alpha}$ direction (TE illumination). Secondly, a plane-wave with the

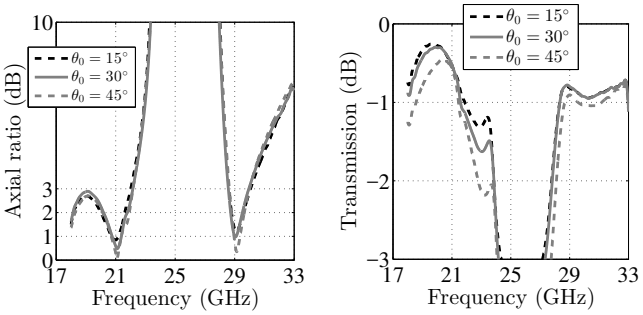

(a) TE illumination (b) TE illumination

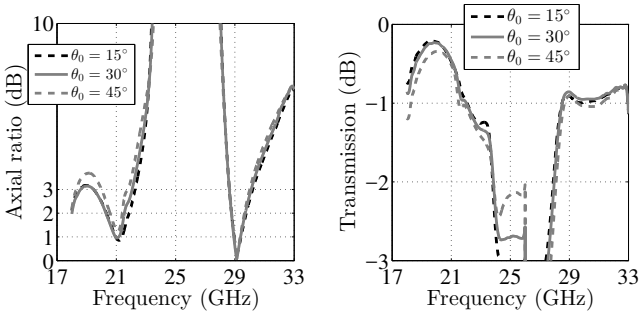

(c) TM illumination (d) TM illumination

Fig. 13. Measured performance of the polarization converter under different incident angles in the βz-plane where $\hat{\beta} = \hat{\alpha} \times \hat{z}$, see Fig. 9. (a)-(c) Axial ratio. (b)-(d) Total transmission. Both vertical (TE) and horizontal (TM) E-field illuminations are considered.

H-field along the $\hat{\alpha}$ direction (TM illumination) is considered. The measured results are shown in Figs. 13(a)-(b) for the TE illumination and in Figs. 13(c)-(d) for the TM.

The AR performance is generally stable for incident angles up to $\pm 45°$. In particular, the 3-dB-AR bandwidths remain roughly unperturbed with respect to normal incidence, when a TE illumination is considered (see Fig. 13(a)). However, Fig. 13(b) shows that the -1-dB-transmission bandwidth slightly narrows with respect to normal incidence.

In general, the measured results differ for TE and TM illuminations. In particular, the TM case is more sensitive to oblique incidences. This is likely due to the asymmetry of the polarizer's unit cell, as depicted in Fig. 6(a)-(b). The 3-dB-AR bandwidth is very stable for angles of incidence up to $\pm 45°$, within the upper frequency band. On the contrary, the lower bandwidth is slightly reduced, as shown in Fig. 13(c). The total efficiency of the polarization converter remains nearly unvaried for all incident angles, as plotted in Figs. 13(d). A detailed and complete summary of the polarizer's performance is reported in Table III for both TE and TM illuminations. The total bandwidth in Table III is calculated as the frequency range where AR $<$ 3 dB and the total transmission is higher than -1 dB. The TM illumination results in narrower bandwidths at lower frequencies, whereas the opposite behavior is observed at higher frequencies. Moreover, the difference between TE and TM illuminations is mitigated at upper frequencies. The coupling effect between the polarizer sheets is, indeed, reduced at those frequencies and a quasi-plane-wave field propagation can be assumed through the metasurfaces.

This article has been accepted for publication in a future issue of this journal, but has not been fully edited. Content may change prior to final publication. Citation information: DOI 10.1109/TAP.2020.2989868, IEEE Transactions on Antennas and Propagation

TABLE III
MEASURED FRACTIONAL BANDWIDTHS OF THE PROPOSED DUAL-BAND, ORTHOGONALLY-POLARIZED LP-TO-CP CONVERTER UNDER OBLIQUE PLANE-WAVE INCIDENCE

TE illumination	$\theta_0 = 15°$		$\theta_0 = 30°$		$\theta_0 = 45°$		
	LHCP	**RHCP**	**LHCP**	**RHCP**	**LHCP**	**RHCP**	
Axial ratio (< 3 dB)	[17, 22]	[28.6, 30]	[17, 22]	[28.6, 30]	[17, 22]	[28.6, 30]	(GHz)
Transmission (> -1 dB)	[18, 21.9]	[28.3, 31]	[18, 21.6]	[28.3, 31]	[18.6, 21.4]	[28.6, 31]	
Total relative bandwidth	19.5	4.8	18.2	4.8	14.0	4.8	(%)

* The total bandwidth refers to the frequency range for which AR < 3 dB and the total transmission is better than -1 dB.

TM illumination	$\theta_0 = 15°$		$\theta_0 = 30°$		$\theta_0 = 45°$		
	LHCP	**RHCP**	**LHCP**	**RHCP**	**LHCP**	**RHCP**	
Axial ratio (< 3 dB)	[19.4, 22.3]	[28.6, 30.2]	[19.4, 22]	[28.6, 30.1]	[20, 21.8]	[28.6, 30.1]	(GHz)
Transmission (> -1 dB)	[18, 22]	[28.5, 31]	[18, 22.04]	[28.5, 31]	[18.3, 21.5]	[28.7, 31]	
Total relative bandwidth	12.5	5.4	12.5	5.1	7.2	4.7	(%)

* The total bandwidth refers to the frequency range for which AR < 3 dB and the total transmission is better than -1 dB.

TABLE IV
COMPARISON WITH STATE-OF-THE-ART DUAL-BAND, ORTHOGONALLY-POLARIZED LP-TO-CP CONVERTERS

Ref.	**Total bandwidths** (%)	**Thickness** (λ)	**Unit cell size** (λ)	**Analytic design**	**Angular stability** (°)
[24], [26]	2.5 and 1.7	0.08	0.37	Quasi	$\pm$30 ***
[25]	14.1 and 8.1	0.13	0.33	No	$\pm$20
[27]	n.a.	0.06	0.41	No	n.a.
[31]	8 and 2.3	1.05	n.a.	No	n.a.
[32]	3.5 and 2.6	1.3 ****	0.57 ****	No	$\pm$5 ***
This work	21.3 and 6	0.26	0.23	Yes	$\pm$45

* The total bandwidths refer to the frequency ranges for which AR < 3 dB and the total transmission is better than -1 dB.
** λ is the free-space wavelength at 25 GHz.
*** This result refers to full-wave simulations only.
**** This result is reported in terms of the free-space wavelength at 15.2 GHz.

D. State-of-the-art comparison

A comparison with state-of-the-art dual-band, orthogonally-polarized LP-to-CP converters for SatCom applications is presented here. Table IV lists some prior articles that proposed a solution to this problem. Our converter represents a good trade-off between performance and size. Polarization conversion is efficiently performed over larger frequency bands with respect to the state-of-the-art. The bandwidths in Table IV refer to frequency bands for which AR < 3 dB and transmission is above -1 dB. As detailed in Section IV-C, the angular stability is also highly improved. Angular stability is dependent on the choice of geometrical shapes for the metasurfaces' unit cells. In fact, the geometries in Fig. 6(a)-(b) mitigate the mutual coupling between the transmitted orthogonal transverse components. Jerusalem's cross-like FSSs are well known for ensuring low sensitivity to oblique incidences [34], [35]. Moreover, the overall thickness of the converter also represents a good trade-off. Ultra-thin polarizers [24], [27] exhibit narrower bandwidths. On the contrary, more complex systems [31], [32] are too bulky. Our polarizer's thickness is electrically-small. The impact of dielectric losses is therefore reduced and high transmission is observed over larger bands. Also, this paper proposes a generic analytic design procedure for dual-band polarizers. In contrast to [24], [26], our method is not dependent on the geometry of the metasurfaces' unit cells. The proposed model allows for the synthesis of dual-band polarizers in terms of generic ECMs. Once the ECMs are obtained, the metasurfaces' unit cells can be designed using various geometries. Analytic formulae also provide insights to overcome the use of multi-parameter optimization processes.

V. IMPACT OF d AND ϵ_r ON AR BANDWIDTHS

In this section, we discuss the impact of the substrate thickness d and dielectric constant ϵ_r on AR bandwidths. The ECMs introduced in Section II avoid using optimizations since ϕ_{01}^{xx} is the only parameter controlled by the designer. This choice enables having an overall view of the maximum achievable performance of the polarizer. For instance, it is sufficient to sweep the value of ϕ_{01}^{xx} and observe the corresponding AR response. However, the simplicity of the model may exclude potential solutions. For instance, other parameters could be used to improve the performance of the design. Here, we consider the substrate's thickness d and dielectric constant ϵ_r as representative example.

In Figs. 14 and 15, the impact of a 20% variation in d and ϵ_r with respect to their design values ($d_{nom} = 1.524$ mm and $\epsilon_{r,nom} = 3.00$) is plotted in terms of AR, respectively. These parameters clearly represent key assets in engineering the 3-dB-AR bandwidth. For instance, Fig. 14(a) shows that larger bandwidths are achieved at higher frequen-

This article has been accepted for publication in a future issue of this journal, but has not been fully edited. Content may change prior to final publication. Citation information: DOI 10.1109/TAP.2020.2989868, IEEE Transactions on Antennas and Propagation

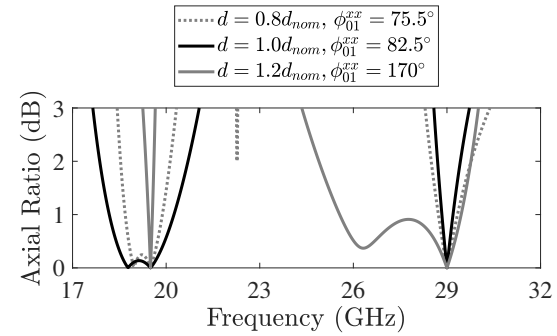

(a) AR for different d.

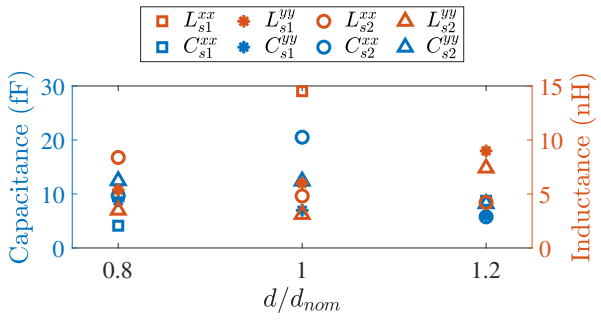

(b) ECMs elements.

Fig. 14. (a) AR versus frequency for different substrate's thicknesses d. (b) Related circuit parameters.

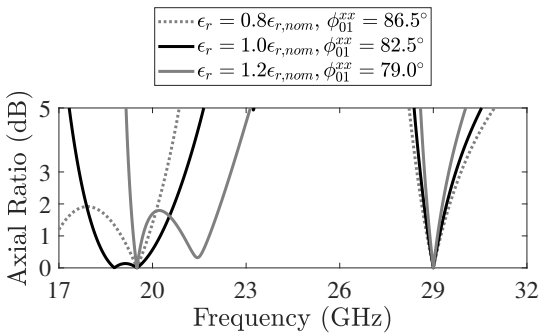

(a) AR for different ϵ_r.

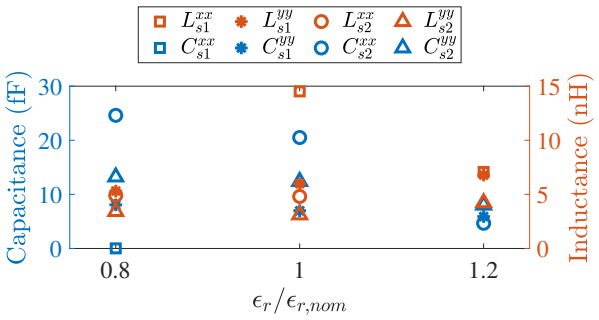

(b) ECMs elements.

Fig. 15. (a) AR versus frequency for different substrate's dielectric constants ϵ_r. (b) Related circuit parameters.

cies when $d = 1.2d_{nom}$. This operating point resembles performance achieved in previous contributions [24], [25]. Likewise, broader 3-dB-AR bandwidths are obtained at lower frequencies when $\epsilon_r = 0.8\epsilon_{r,nom}$ or $\epsilon_r = 1.2\epsilon_{r,nom}$ (see Fig. 15(a)).

Using d and ϵ_r as design parameters may impact the overall design of the structure. One issue is the physical implementation of ECM's elements. The range of values of ECM's entries is dependent on the geometry of the metasurfaces' unit cells. Assuming a given unit cell geometry, only a limited range of circuit element values can be realized. To give an example, the geometry in Fig. 6(a) and (b) can realize capacitance and inductance in the range of [6.5, 25] (fF) and [2.5,15] (nH), respectively. As shown in Fig. 14(b) and 15(b), the design complexity fairly increases for $d = 0.8d_{nom}$ and $\epsilon_r = 0.8\epsilon_{r,nom}$, since the capacitance C_{s1}^{xx} reaches very low values. In this scenario, the geometries in Fig. 6(a) and (b) cannot be employed in the physical design. Different geometries can obviously help in overcoming this issue. Nonetheless, the set of usable geometries is limited, given the electrically-small unit cell's size at K/Ka-band. Finally, fabrication constraints represent a further limitation in the implementation of the circuit elements.

Moreover, it is worth mentioning that Figs. 14 and 15 report results around the operating point $(d_{nom}, \epsilon_{r,nom})$. In this scenario, $(d, \epsilon_r) = (d_{nom}, \epsilon_{r,nom})$ represents the optimal choice for a variation of d and ϵ_r up to 20%. This does not mean that a better operating point cannot be achieved by optimizing d, ϵ_r and ϕ_{01}^{xx} over larger ranges. One could possibly trade off a better performance for increased computational complexity. This is something that will be explored in future work.

VI. Conclusion

A novel design method for dual-band, orthogonally-polarized linear-to-circular polarization converters is proposed in this contribution. The polarization converter consists of three cascaded sheet admittances, separated by two dielectric slabs. Each sheet admittance is modeled using equivalent circuit models based on periodically-loaded transmission lines. By enforcing 100% transmission at two separate frequencies, the equivalent circuit models of the polarization converter are described by means of closed-form analytic expressions. The bandwidths of the polarizer are thus engineered according to specifications. The proposed method avoids the use of multi-parameter optimizations. A dual-band, orthogonally-polarized linear-to-circular polarization converter is designed in the K/Ka-band for satellite communication applications. A prototype was fabricated in printed circuit board technology. Measurements were performed to validate the numerical results. The measured results are in very good agreement with full-wave simulations. Under normal incidence, the polarizer efficiently performs linear-to-left-hand-circular polarization conversion over the band 18-22.2 GHz ($\sim 21\%$). In addition, linear-to-right-hand-circular polarization conversion is demonstrated in the band 28.7-30.4 GHz ($\sim 6\%$). These bandwidths are calculated as the frequency ranges over which the axial ratio is below 3 dB and the transmission is above -1 dB. The polarizer performance remains stable under oblique incidence for angles up to $\pm 45°$. The axial ratio remains lower

This article has been accepted for publication in a future issue of this journal, but has not been fully edited. Content may change prior to final publication. Citation information: DOI 10.1109/TAP.2020.2989868, IEEE Transactions on Antennas and Propagation

than 3 dB over the bands 17-22 GHz ($\sim 25.6\%$) and 28.6-30 GHz ($\sim 4.7\%$) when the plane-wave's incident angle is 45°. Furthermore, the insertion loss remains lower than 1.2 dB in this scenario. Such a device may find application in satellite communication terminals for polarization control based on its low profile and stable performances with scanning. For instance, it can be integrated with linearly-polarized satellite communication terminal antennas to enhance robustness and isolation between transmitted and received signal.

ACKNOWLEDGMENT

The authors would like to thank dr. Laurent Le Coq and Frederic Boutet for their help in performing the the measurements.

APPENDIX A
DERIVATION OF Y_{s1} AND Y_{s2} IN CLOSED FORM

This appendix details the derivation of equations (4) and (5). A scalar formulation is used to streamline the notation. The network is assumed to be symmetric, reciprocal and lossless. Under this assumption, the following relation holds [15]

$$\xi = det\left\{\begin{bmatrix} A_1 & B_1 \\ C_1 & D_1 \end{bmatrix}\right\} = A_1 D_1 - B_1 C_1 = 1 \tag{IA.1}$$

where A_1, B_1, C_1 and D_1 are defined in (3). Their extended form is given by

$$A_1 = \cos\theta \tag{IA.2}$$

$$B_1 = i\eta_d \sin\theta \tag{IA.3}$$

$$C_1 = Y_{s1}\cos\theta + \frac{i\sin\theta}{\eta_d} \tag{IA.4}$$

$$D_1 = iY_{s1}\eta_d \sin\theta + \cos\theta \tag{IA.5}$$

A. Closed form of Y_{s1}

The unit cell in Fig. 2 is assumed infinitely-periodic along z-axis. This allows a Bloch phase delay ϕ and the Bloch impedance Z_B to be defined. The Bloch impedance Z_B can be expressed in terms of an $ABCD$ matrix formulation [15], yielding

$$Z_B = \frac{-iB}{D\tan\phi} \tag{IA.6}$$

where A, B, C and D are defined in (2). Using the matrix multiplication, they can be written as

$$A = \frac{1}{\xi}(A_1 D_1 + B_1 C_1 + B_1 D_1 Y_{s2}) \tag{IA.7}$$

$$B = \frac{1}{\xi}(2A_1 B_1 + B_1^2 Y_{s2}) \tag{IA.8}$$

$$C = \frac{1}{\xi}(2C_1 D_1 + D_1^2 Y_{s2}) \tag{IA.9}$$

$$D = A \tag{IA.10}$$

The Bloch phase delay can be found as function of the $ABCD$ matrix entries [15], yielding

$$\cos\phi = A = A_1 D_1 + B_1 C_1 + B_1 D_1 Y_{s2} \tag{IA.11}$$

Exploiting (IA.1), the relation (IA.11) reduces to

$$\cos\phi = 2A_1 D_1 + B_1 D_1 Y_{s2} - 1 \tag{IA.12}$$

and can be arranged in the following form:

$$\frac{1+\cos\phi}{D_1} = 2A_1 + B_1 Y_{s2} \tag{IA.13}$$

Now, we can focus on finding the expression of the Bloch impedance Z_B as function of the Bloch phase delay ϕ, the $ABCD$ matrix and Y_{s2}, by substituting (IA.8) and (IA.10) into (IA.6). In formulae [16]:

$$Z_B = \frac{-iB_1(2A_1 + B_1 Y_{s2})}{(A_1 D_1 + B_1 C_1 + B_1 D_1 Y_{s2})\tan\phi} \tag{IA.14}$$

By substituting (IA.11) and (IA.13) into (IA.14), we obtain

$$Z_B = \frac{-iB_1(1+\cos\phi)}{D_1\cos\phi\tan\phi} = \frac{-iB_1}{D_1\tan(\phi/2)} \tag{IA.15}$$

where the trigonometric identity $\frac{1+\cos\phi}{\cos\phi\tan\phi} = \frac{1}{\tan(\phi/2)}$ was used.

By inserting (IA.3) and (IA.5) into (IA.15), the following relation is found

$$Z_B = \frac{\eta_d \sin\theta}{(iY_{s1}\eta_d \sin\theta + \cos\theta)\tan(\phi/2)} \tag{IA.16}$$

Finally, (4) is obtained by inverting (IA.16) and applying some algebraic manipulations.

B. Closed form of Y_{s2}

By inserting (IA.2) and (IA.3) into (IA.8) and using the relation (IA.1), the second entry B of the overall $ABCD$ matrix takes the following form

$$B = i\eta_d \sin(2\theta) - Y_{s2}\eta_d^2 \sin^2\theta \tag{IA.17}$$

Furthermore, B can be expressed in terms of the Bloch unit cell's phase delay ϕ and Bloch impedance Z_B [15], yielding

$$B = iZ_B \sin\phi \tag{IA.18}$$

Y_{s2} is found by equating (IA.17) and (IA.18), yielding

$$Y_{s2} = \frac{i}{\eta_d}\left(\frac{\sin(2\theta)}{\sin^2\theta} - \frac{Z_B}{\eta_d}\csc^2\theta\sin\phi\right) \tag{IA.19}$$

Finally, equation (5) is obtained using the following trigonometric identity: $\frac{\sin(2\theta)}{\sin^2\theta} = 2\cot\theta$.

REFERENCES

[1] R. Dybdal, "Communication satellite antennas: system architecture, technology, and evaluation.", McGraw-Hill, 2009.

[2] H. Bayer, A. Krauss, T. Zaiczek, R. Stephan, O. Enge-Rosenblatt, and M. A. Hein, "Ka-band user terminal antennas for satellite communications," *IEEE Trans. Antennas Propag.*, vol. 58, no. 1, pp. 7688, Feb. 2016.

[3] R. A. Pearson, J. Vazquez, M. W. Shelley, A. Payne, V. Stoiljkovic, and M. Steel, "Next generation mobile SATCOM terminal antennas for a transformed world," *Proc. 5th Eur. Conf. Antennas Propag. (EuCAP)*, Rome, 2011, pp. 2341-2345.

[4] A. V. Stankovsky, Y. A. Litinskaya, A. M. Alexandrin, S. V. Polenga, and Y. P. Salomatov, "Spatial polarizers for CTS structure-based antenna arrays," *2019 IEEE Conference of Russian Young Researchers in Electrical and Electronic Engineering (EIConRus)*, Saint Petersburg and Moscow, Russia, 2019, pp. 885-889.

[5] M.-A. Joyal, and J.-J. Laurin, "Analysis and design of thin circular polarizers based on meander lines," *IEEE Trans. Antennas Propag.*, vol. 60, no. 6, pp. 3007-3011, Jun. 2012.

[6] S. M. A. Momeni Hasan Abadi, and N. Behdad, "Wideband linear-to-circular polarization converters based on miniaturized-element frequency selective surfaces," *IEEE Trans. Antennas Propag.*, vol. 64, no. 2, pp. 525-534, Feb. 2016.

[7] L. Martinez-Lopez, J. Rodriguez-Cuevas, J. I. Martinez-Lopez, and A. E. Martynyuk, "A multilayer circular polarizer based on bisected split-ring frequency selective surfaces," *IEEE Antennas Wireless Popag. Lett.*, vol. 13, pp. 153-156, 2014.

[8] M. Hosseini, and S. V. Hum, "A circuit-driven design methodology for a circular polarizer based on modified Jerusalem cross grids," *IEEE Trans. Antennas Propag.*, vol. 65, no. 10, pp. 5322-5331, Oct. 2017.

[9] F. F. Manzillo, M. Ettorre, R. Sauleau and, A. Grbic, "Systematic design of a class of wideband circular polarizers using dispersion engineering," *11th Eur. Conf. Antennas Propag. (EUCAP)*, Paris, 2017, pp. 1279-1281.

[10] M. A. Antoniades, and G. V. Eleftheriades, "Compact linear lead/lag metamaterial phase shifters for broadband applications," *IEEE Antennas Wireless Popag. Lett.*, vol. 2, pp. 103-106, 2003.

[11] M. A. Antoniades and, G. V. Eleftheriades, "A broadband Wilkinson balun using microstrip metamaterial lines," *IEEE Antennas Wireless Popag. Lett.*, vol. 4, pp. 209-212, 2005.

[12] M. Born, and E. Wolf, "Principles of optics, 7th ed.," Cambridge University Press, 1999.

[13] C. Pfeiffer and A. Grbic, "Millimeter-wave transmitarrays for wavefront and polarization control," *IEEE Trans. Microw. Theory Tech.*, vol. 61, no. 12, pp. 4407-4417, Dec. 2013.

[14] C. Pfeiffer, and A. Grbic, "Bianisotropic metasurfaces for optimal polarization control: analysis and synthesis," *Phys. Rev. Applied*, vol. 2, pp. 044011, Oct. 2014.

[15] D. M. Pozar, "Microwave engineering - 3th ed.," John Wiley & Sons, 2005.

[16] A. Grbic, "Super-resolving negative-refractive-index transmission-line lenses," Ph.D. dissertation, University of Toronto, Toronto, Canada, 2006.

[17] N. Marcuvitz, "Waveguide handbook," McGraw-Hill, 1951.

[18] B. A. Munk, "Frequency selective surfaces: theory and design," John Wiley & Sons, Inc., 2000.

[19] P. Naseri, and S. V. Hum, "A dual-band dual-circularly polarized reflectarray for K/Ka-band space applications," *2019 13th Eur. Conf. Antennas Propag. (EuCAP)*, Krakow, Poland, 2019, pp. 1-5.

[20] P. Naseri, M. Riel, Y. Demers, and S. V. Hum, "A dual-band dual-circularly polarized reflectarray for K/Ka-band space applications," *IEEE Trans. Antennas Propag.*, 2020.

[21] N. J. G. Fonseca, and C. Mangenot, 'Low-profile polarizing surface with dual-band operation in orthogonal polarizations for broadband satellite applications," *2014 8th Eur. Conf. Antennas Propag. (EuCAP)*, The Hague, 2014, pp. 471-475.

[22] N. J. G. Fonseca, and C. Mangenot, "High-performance electrically thin dual-band polarizing reflective surface for broadband satellite applications," *IEEE Trans. Antennas Propag.*, vol. 64, no. 2, pp. 640-649, Feb. 2016.

[23] W. Tang, S. Mercader-Pellicer, G. Goussetis, H. Legay, and N. J. G. Fonseca, "Low-profile compact dual-band unit cell for polarizing surfaces operating in orthogonal polarizations," *IEEE Trans. Antennas Propag.*, vol. 65, no. 3, pp. 1472-1477, March 2017.

[24] P. Naseri, S. A. Matos, J. R. Costa, C. A. Fernandes, and N. J. G. Fonseca, "Dual-band dual-linear-to-circular polarization converter in transmission mode application to K/Ka-band satellite communications," *IEEE Trans. Antennas Propag.*, vol. 66, no. 12, pp. 7128-7137, Dec. 2018.

[25] H. B. Wang, and Y. J. Cheng, "Single-layer dual-band linear-to-circular polarization converter with wide axial ratio bandwidth and different polarization modes," *IEEE Trans. Antennas Propag.*, vol. 67, no. 6, pp. 4296-4301, Jun. 2019.

[26] P. Naseri, J. R. Costa, S. A. Matos, C. A. Fernandes, and S. V. Hum, "Equivalent circuit modeling to design a dual-band dual linear-to-circular polarizer surface," *IEEE Trans. Antennas Propag., 2020*

[27] H. Cao, X. Wu, Y. Pi, J. Liu, H. Xu, Z. Meng, Y. Yu, and J. Fan, "A novel chiral metamaterial circular polarizer based on e-shaped structure," *Proc. Antennas Propag. Symp. (APS)*, Fajardo, Puerto Rico, July 2016.

[28] Advanced Design System (ADS), www.keysight.com.

[29] A. Ranjbar, and A. Grbic, "Analysis and synthesis of cascaded metasurfaces using wave matrices", *Phys. Rev. B.*, vol. 95, no. 12, pp. 205114, May 2017.

[30] A. Ranjbar, and A. Grbic, "Broadband, multiband, and multifunctional all-dielectric metasurfaces", *Phys. Rev. Applied*, vol. 11, no. 5, pp. 054066, May 2019.

[31] E. Arnieri, F. Greco, L. Boccia, and G. Amendola, "A SIW-based polarization rotator with an application to linear-to-circular dual band polarizers at K/Ka band," *IEEE Trans. Antennas Propag.*, 2020.

[32] C. Molero, E. Menargues, and M. García-Vigueras, "All-metal 3-D frequency selective surface with versatile dual-band polarization conversion," *IEEE Trans. Antennas Propag.*, 2020.

[33] Z. Wu, Y. Ra'di, and A. Grbic, "Tunable metasurfaces: a polarization rotator design," *Phys. Rev. X*, vol. 9, no. 15, pp. 011036, Feb. 2019.

[34] Tian-Wu Li, Da Li, and Er-Ping Li, "A novel FSS structure with high selectivity and excellent angular stability for 5G communication radome," *2017 10th Global Symposium on Millimeter-Waves*, Hong Kong, 2017, pp. 50-52.

[35] M. Hosseini, A. Pirhadi, and M. Hakkak, "A novel AMC with little sensitivity to the angle of incidence using 2-layer jerusalem cross FSS," *Progress Electromagnetics Research*, vol. 64, 43-51, 2006.

[36] ANSYS Electronics Desktop 2018.2, HFSS High-frequency structure simulation, 2018.

[37] R. J. Langley, and A. J. Drinkwater, "Improved empirical model for the Jerusalem cross," *IEE Proceedings H - Microwaves, Optics and Antennas*, vol. 129, no. 1, pp. 1-6, Feb. 1982.

[38] F. Costa, A. Monorchio, and G. Manara, "Efficient analysis of frequency-selective surfaces by a simple equivalent-circuit model," *IEEE Antennas Propag.*, vol. 54, no. 4, pp. 35-48, Aug. 2012.

[39] Thomas Keating Ltd, www.terahertz.co.uk.

[40] Rogers Corporation, https://www.rogerscorp.com.